JM PAPERS

Wave scattering by a three-dimensional submerged horizontal rectangular plate in a channel: experiments and numerical computations

T. Geng[1], H. Liu[2], Q. Wang[2] and F. Dias[1,3],†

[1] School of Mathematics and Statistics, University College Dublin, Belfield, Dublin, Ireland

[2] Department of Engineering Mechanics, Shanghai Jiao Tong University, PR China

[3] ENS Paris-Saclay, CNRS, Centre Borelli, Université Paris-Saclay, Gif-sur-Yvette 91190, France

Experiments are conducted in a wave tank to investigate wave scattering by a three-dimensional submerged horizontal rectangular plate in a channel. The free-surface elevation around the plate is presented for various water depths and depths of submergence of the plate. The wave forces and moments are obtained using an underwater load measuring system. The numerical simulations are performed with a parallelized three-dimensional boundary element method. The numerical set-up follows closely the set-up of the laboratory experiments. The numerical results are compared with the experimental results for non-breaking waves. In most cases a good agreement is found for the free-surface elevation, the vertical force and the moment. A physical interpretation of the flow around the plate is provided. The pressure distribution on the lower surface of the plate differs from the linear distribution from the leading edge to the trailing edge that is obtained in the equivalent two-dimensional problem. The reflection by the lateral walls is investigated.

Key words: wave scattering, wave-structure interactions

1. Introduction

The interaction of a solitary wave with a three-dimensional (3-D) submerged horizontal plate in a channel was recently investigated experimentally by Wang *et al.* (2020) and numerically by Geng, Liu & Dias (2021). It was shown that when the wave approaches or leaves the plate, the channel flow underneath the plate contributes to the positive

† Email address for correspondence: frederic.dias@ucd.ie

peaks of the vertical force. As the wave crest approaches the centre of the plate, the negative force caused by the dynamic pressure on the upper surface of the plate dominates. Here we consider again the propagation of waves above a submerged horizontal plate in a channel but from the point of view of wave scattering. The incoming waves are nonlinear periodic waves. The problem of wave scattering by a submerged plate has been widely studied. In the framework of linear potential wave theory, the method of matched asymptotic expansions was applied by Siew & Hurley (1977) to give the first-order reflection and transmission coefficients for the scattering of long waves by a submerged plate. Patarapanich (1984) studied numerically forces and moments exerted on the plate by using a finite element method and then compared the results with those of Siew and Hurley. Patarapanich & Cheong (1989) conducted experiments and reported optimal conditions for the submerged horizontal plate to minimize the wave transmission. The method of eigenfunction expansion was used by Liu & Iskandarani (1991) to study short-wave scattering by a submerged plate. This method was extended by Cheong, Shankar & Nallayarasu (1996) to the complete range of water depths. Dong *et al.* (2018) further modified the method to allow for a varying bathymetry. Another approach to study the problem is to use an integral equation method. Parsons & Martin (1992) investigated the variation of the reflection coefficient as a function of the angle of inclination of the plate by using hypersingular integral equations.

The study of nonlinear effects is relatively scarce. Kojima, Yoshida & Nakamura (1994) reported nonlinear wave forces exerted on a submerged horizontal plate to the second order. Brossard & Chagdali (2001) presented an experimental study of higher harmonics induced by a submerged plate. Two moving wave probes were used to separate the reflected waves from the incident waves. Liu, Huang & Tan (2009) developed a desingularized boundary element method (BEM) to study the nonlinear wave scattering by a submerged thin plate. Higher harmonics were extracted and compared with experimental results from Brossard & Chagdali (2001). Simulations based on the Navier–Stokes equations can also be found. Pinon *et al.* (2017) used a two-dimensional (2-D) Lagrangian vortex method to study the velocity and vorticity field around the plate. The numerical work was the continuation of the experimental study by Poupardin *et al.* (2017).

For the 3-D case, several methods have been used to study wave scattering by a submerged circular disk due to the simplicity of its shape. Yu & Chwang (1993) proposed a theoretical solution to the problem using an eigenfunction expansion approach. They investigated the phenomenon of wave focusing behind the plate. Farina & Martin (1998) studied this problem in deep water and reduced it to a hypersingular integral equation over the surface of the disc. They discussed the relationship between the scattering cross-section and the added mass. Both cases are restricted to open-sea conditions and a circular shape. However, when the structures are located inside a harbour or some naturally formed confined offshore area, the scattered waves are reflected by the lateral walls and interact with the incoming waves. In the present paper, we describe a series of experiments that were conducted in the Tsunami Basin for Offshore Regions (Wang, Fang & Liu 2018) to better understand how the lateral walls on both sides of the channel affect the wave field. A thorough investigation of wave scattering by a 3-D submerged rectangular plate is performed. Numerical simulations, which use a parallelized fully nonlinear BEM, are performed to compare and further explore the phenomena observed in the experiments. Both the experiments and the numerical simulations are novel.

The main objective of this paper is to investigate the loads on the submerged horizontal plate. The layout of the paper is as follows. In § 2, we review the experiments. The numerical method is then briefly described in § 3. Section 4 provides comparisons of the numerical results with the experimental results for the free-surface elevation, the forces
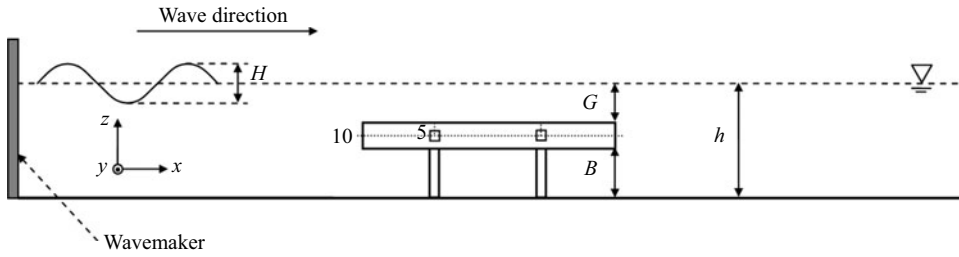
Figure 1. Side view of the wave flume and plate used for the laboratory experiments. The parameters that can be adjusted in the experiments are the wave height H, the water depth h, the distance from the bottom to the lower surface of the plate B and the depth of submergence of the plate G. The plate is 10 cm thick.

and the moments. A parametric study is performed. Conclusions and a discussion of our results are presented in § 5.

2. Description of the experiments

The experiments were conducted in the Tsunami Basin for Offshore Regions in Shanghai Jiao Tong University. A detailed description of the set-up is provided by Wang *et al.* (2020). Even though Wang *et al.* (2020) focus on solitary waves, the experimental set-up is the same. In the experiments, each case is repeated three times. The maximum relative error is less than 5 %. The standard deviation is from 1 % to 2.6 %. In general, the smaller the wave amplitude, the larger the statistical error probably caused by electrical noise. The wave flume is 42 m long and 4 m wide with a piston-type wavemaker installed at one end. The plate-type structure is made of organic glass. It is 200 cm long, 78 cm wide, 10 cm thick and mounted on the bottom in the middle region of the flume (see figure 1). Four piezoelectric force balance units are installed inside the plate. A dynamometric system is used to measure wave loads on the structure. The constant water depth is denoted by h.

The free-surface elevation is measured by resistance-type wave gauges (WGs). Twenty WGs are spread around the plate; their exact locations and labels are shown in figure 2. Taking the centre of the plate as the origin $(0, 0)$ of the horizontal (x, y)-plane, we list the (x, y)-coordinates of all the WGs in table 1.

We use the classical wavemaker theory for plane waves produced by a piston-type wavemaker; it is explained, for example, by Dean & Dalrymple (1991). Time is denoted by t. The wave produced by the wavemaker propagates along the positive x-direction. To obtain a periodic wave elevation $\eta(x, t)$ with wave height H, wavenumber k and angular frequency ω (or period $T = 2\pi/\omega$), that behaves like

$$\eta(x, t) = \frac{H}{2} \cos(kx - \omega t) \tag{2.1}$$

far away from the wavemaker, the horizontal displacement $s(t)$ of the wavemaker must be defined by

$$s(t) = \frac{S}{2} \sin \omega t, \tag{2.2}$$

where S is the stroke of the wavemaker.
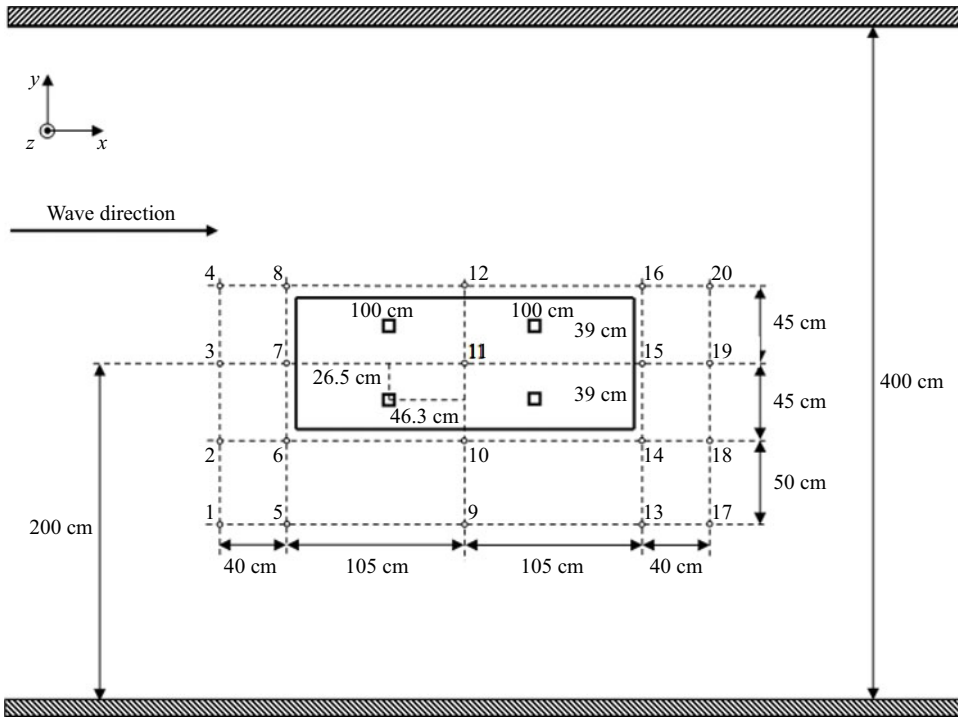
Figure 2. Top view of the wave flume and plate used for the laboratory experiments (all distances are in cm). The locations of the 20 WGs, labelled 1 to 20, are shown. They lie along four lines in the direction of the wave and five lines across the wave flume. The four squares indicate the locations of the four three-component force balance units.

WG1	$(-145, -95)$	WG5	$(-105, -95)$	WG9	$(0, -95)$	WG13	$(105, -95)$	WG17	$(145, -95)$
WG2	$(-145, -45)$	WG6	$(-105, -45)$	WG10	$(0, -45)$	WG14	$(105, -45)$	WG18	$(145, -45)$
WG3	$(-145, 0)$	WG7	$(-105, 0)$	WG11	$(0, 0)$	WG15	$(105, 0)$	WG19	$(145, 0)$
WG4	$(-145, 45)$	WG8	$(-105, 45)$	WG12	$(0, 45)$	WG16	$(105, 45)$	WG20	$(145, 45)$

Table 1. Coordinates of the twenty WGs (in cm). The coordinates $(0, 0)$ correspond to the centre of the plate.

The ratio of wave height to stroke is given by

$$\frac{H}{S} = \frac{2(\cosh 2kh - 1)}{\sinh 2kh + 2kh},$$

(2.3)

where the wavenumber k satisfies the dispersion relation

$$\omega^2 = gk \tanh kh.$$

(2.4)

3. Numerical method

Numerical models of 3-D potential flow wave propagation can be divided into three main categories: (i) BEMs; (ii) finite element methods; (iii) spectral methods. Methods (i) and (iii) reduce the water wave problem from one posed inside the entire fluid domain to one posed on the boundary alone, thus reducing the dimension of the formulation.
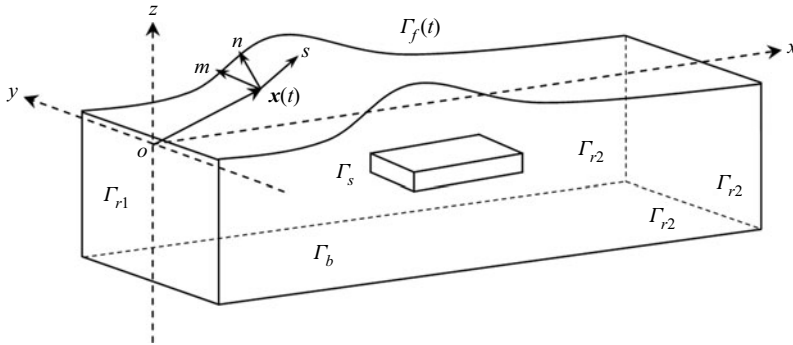
Figure 3. Sketch of the computational domain. The free surface $\Gamma_f(t)$ is defined by the position vector $x(t)$. Lateral boundaries are denoted by Γ_{r1} and Γ_{r2}, where Γ_{r1} is the boundary for the wavemaker and Γ_{r2} are other impermeable walls. The bottom and the structure are denoted by Γ_b and Γ_s, respectively. Tangential vectors at point $x(t)$ are defined as (s, m) and the outward normal vector as n.

These approaches are summarized for example in Grilli *et al.* (2010). The present study uses a boundary element numerical wave tank (known as NWT) code, which has already been used by Geng *et al.* (2021). The code uses a BEM to compute field variables. The 16-node quadrilateral elements provide global third-order precision. Since the numerical wave tank was fully explained in Geng *et al.* (2021), we only provide a summary of the main features (see also Grilli *et al.* 2001).

3.1. *Mathematical formulation*

The computational domain is shown in figure 3. The velocity potential $\phi(x, t)$ is used to represent the 3-D flow, which is assumed to be inviscid and irrotational. Here $x = (x, y, z)$ denotes a point inside the fluid domain, with z the vertical coordinate. The continuity equation in the fluid domain is the 3-D Laplace's equation for ϕ, i.e.

$$\nabla^2 \phi = 0. \tag{3.1}$$

Green's second identity transforms Laplace's equation (3.1) into an integral equation on the boundary,

$$\alpha(x_l)\phi(x_l) = \int_\Gamma \left\{ \frac{\partial \phi}{\partial n}(x)G(x, x_l) - \phi(x)\frac{\partial G}{\partial n}(x, x_l) \right\} d\Gamma, \tag{3.2}$$

where x and x_l are the coordinates of points on the boundary, G is the 3-D free space Green's function $G(x, x_l) = 1/4\pi r$ and $(\partial G/\partial n)(x, x_l) = -(1/4\pi)(r \cdot n/r^3)$, $\partial/\partial n$ is the normal derivative with the normal vector pointing out of the domain and $\alpha(x_l)$ is proportional to the exterior solid angle made by the boundary at the collocation point x_l. The boundary Γ consists of the free surface, the flat bottom, the six sides of the submerged horizontal plate, the wavemaker and the end of the wave tank.

At a point x on the free surface, ϕ satisfies the nonlinear kinematic and dynamic boundary conditions, written in a mixed Eulerian–Lagrangian form, with the material derivative $D/Dt \equiv \partial/\partial t + \nabla\phi \cdot \nabla$, as follows:

$$\frac{Dx}{Dt} = \nabla\phi, \tag{3.3}$$

$$\frac{D\phi}{Dt} = -gz + \frac{1}{2}\nabla\phi \cdot \nabla\phi, \tag{3.4}$$

where g is the acceleration due to gravity. At the wavemaker moving with velocity U, the normal velocity is continuous over the surface of the wavemaker,

$$\frac{\partial \phi}{\partial n} = U \cdot n. \tag{3.5}$$

At the bottom and other fixed parts of the boundary, the no-flow condition $\partial \phi / \partial n = 0$ is prescribed.

3.2. *Time integration*

Second-order explicit Taylor series expansions are used to express both the new position and potential on the free surface. First-order coefficients are given by the boundary conditions (3.3) and (3.4). The pairs $\partial \phi / \partial t$, $\partial^2 \phi / \partial t \partial n$ are computed by solving another integral equation similar to (3.2). For the evaluation of the tangential derivatives, a fourth-order interpolation scheme is employed.

The time step is adapted by finding the minimum distance between two nodes on the free surface. In order to maintain the stability when strong nonlinear free-surface deformations occur, an equally spaced regridding method is adopted every 10 time steps, starting when the first wavefront arrives at the leading edge of the plate.

3.3. *Spatial discretization*

The boundary is discretized into N collocation nodes and M high-order elements are used to interpolate in-between q of these nodes. Within each element, the boundary geometry and the field variables are discretized using polynomial shape functions. We choose cubic reference elements ($q = 16$), which provides C_2 continuity in-between elements.

The integral equation (3.2) is transformed into a sum of integrals over the boundary elements, each one being calculated on the reference element. The associated discretized boundary integral equation leads to a sum on the N boundary nodes,

$$\alpha(x_l)\phi(x_l) = \sum_{j=1}^{N} \left(K_{lj}^D \frac{\partial \phi}{\partial n}(x_j) - K_{lj}^N \phi(x_j) \right), \tag{3.6}$$

where $l = 1, \ldots, N$. Here K_{lj}^D and K_{lj}^N are Dirichlet and Neumann global matrices, respectively.

In terms of the intersecting parts of different boundaries, such as between the free surface and the lateral boundary, boundary conditions and normal directions are generally different. Therefore, double nodes are used to represent these corners and the continuity of the potential is imposed.

3.4. *Convergence*

A convergence test is conducted using meshes with three different resolutions. Table 2 shows the number of nodes on the free surface. A comparison of the results is shown in figure 4. It can be seen that the numerical results obtained using mesh 2 are close to those from mesh 3 but slightly deviate from those obtained using mesh 1. Therefore, mesh 2 is considered to be sufficient to reach a convergent solution in our model.
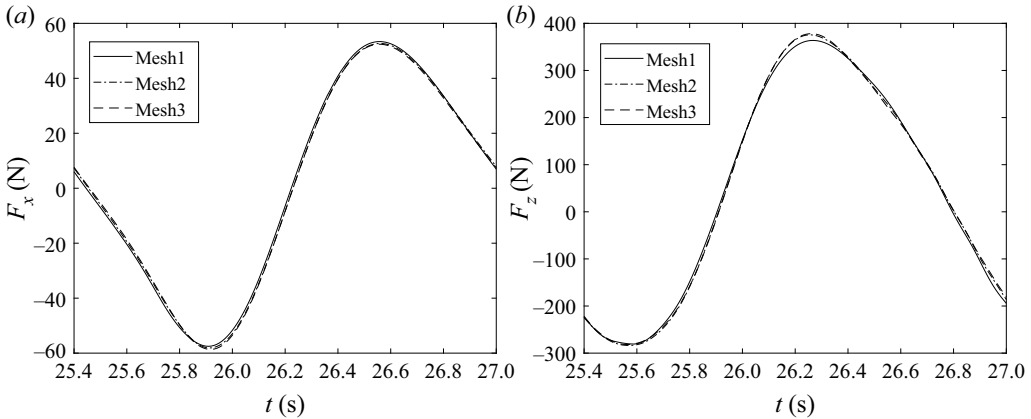
Figure 4. Comparison of the hydrodynamic load on the plate as a function of time t with three different mesh resolutions. (*a*) Horizontal force F_x; (*b*) vertical force F_z.

Mesh no.	Number of nodes
1	3856
2	6321
3	9386

Table 2. Number of nodes for different meshes on the free surface tested for convergence.

3.5. *Wave generation*

For the numerical wave generation, a simple exponential ramp function is applied on the horizontal displacement $s(t)$ provided by (2.2) to make the generation smooth. A similar method can be found in Yan & Ma (2007) and Liam, Adytia & van Groesen (2014),

$$s(t) = \frac{S}{2} \sin \omega t (1 - e^{-\beta \omega t}), \tag{3.7}$$

where β is a constant that was adapted for the various periods we considered.

How the wavemaker is ramped exactly in the experiment is unknown. Therefore, a slight deviation between the numerical and experimental results is expected at the beginning.

4. Results

As shown in figure 1, G is the depth of submergence and B is the distance from the bottom to the lower surface of the plate. Two different water depths ($h = 50$ and 60 cm) and three depths of submergence ($G = 20$, 30 and 40 cm) were used in the laboratory experiments. For each combination of h and B, three different ratios of wave height to water depth were investigated. Finally, for each ratio, five different wave periods ($T = 1.2$, 1.4, 1.6, 1.8 and 2.0 s) were tested. The combinations are summarized in table 3.

The set of experiments contained both non-breaking and breaking cases. The list of non-breaking cases is provided in table 4. Since the boundary integral equation method cannot handle broken waves, the comparison with experiments involving broken waves is left for future work. Note that in some cases that are borderline between breaking and

B (cm)	h (cm)	B (cm)	h (cm)	B (cm)	h (cm)
20	50/60	30	50/60	40	60

Table 3. Experimental cases. For each combination of B and h, there are three values of the ratio of wave height to water depth H/h (0.1, 0.2 and 0.3) and five values of the period T (1.2, 1.4, 1.6, 1.8 and 2.0 s).

B (cm)	h (cm)	H/h	T (s)	H/L
20	50	0.1	1.2, 1.4, 1.6, 1.8, 2.0	0.0244, 0.0195, 0.0163, 0.0140, 0.0123
	50	0.2	1.2, 1.4, 1.6, 1.8, 2.0	0.0489, 0.0389, 0.0325, 0.0280, 0.0247
	60	0.1	1.2, 1.4, 1.6, 1.8, 2.0	0.0283, 0.0222, 0.0184, 0.0157, 0.0138
	60	0.2	1.2, 1.4, 1.6, 1.8, 2.0	0.0566, 0.0444, 0.0367, 0.0314, 0.0275
	60	0.3	1.4, 1.6, 1.8, 2.0	0.0666, 0.0551, 0.0471, 0.0413
30	60	0.1/0.2	1.2, 1.4, 1.6, 1.8, 2.0	

Table 4. Non-breaking experimental cases.

non-breaking, the numerical simulations led to wave breaking while no wave breaking was observed during the experiments.

4.1. *Surface elevation*

In this section, the free-surface elevation at selected WGs, normalized by the wave height H, is compared with experimental measurements. The numerical and experimental results are synchronized using the data of WG3, which is located on the middle line upstream of the plate. When WGs are symmetrically located, like WG2 and WG4, the results of only one WG are shown below. In fact, these WGs were used to check the symmetry of the measurements.

Figure 5 shows comparisons between experimental and numerical results in the case $B = 20$ cm, $h = 50$ cm, $H/h = 0.1$ at six selected WGs (five of them, WG3, 7, 11, 15, 19, are along the x-axis, which coincides with the centreline of the plate; WG13 is off one of the downstream edges of the plate) for three different wave periods (1.2 s, 1.6 s, 2 s). Figure 6 is the same as figure 5, except that $B = 30$ cm, $h = 60$ cm, $H/h = 0.2$. Unfortunately the physical wavemaker software package that includes the algorithm used to generate the regular waves is a 'black box'. Even though the time ramp used in the experiments to gradually generate the waves is different from the algorithm used in the numerical simulations, the overall agreement is uniformly good. It can been seen that the wave amplitudes are not always constant. For example, in figure 5, the free-surface elevation at WG11 decreases as a function of time for $T = 1.2$ s while it increases for $T = 2$ s. The wave amplitude also increases at WG7 for $T = 1.2$ s. The free-surface elevations at WG3 and WG7 for $T = 2$ s even decrease first before increasing again. At WG19 for $T = 1.2$ s, the wave amplitude first increases and then plateaus at a constant value. These changing wave amplitudes are the result of the interaction between the reflected scattered waves from the lateral walls and the incoming wave. The varying wave field above the plate has a great influence on the hydrodynamic loads on the plate, especially the vertical force.

Due to shoaling, the wave amplitude at WG11, which is the only WG located above the plate, is normally the largest and can be as large as two to three times the incoming wave amplitude depending on the depth of submergence. However, in the middle column
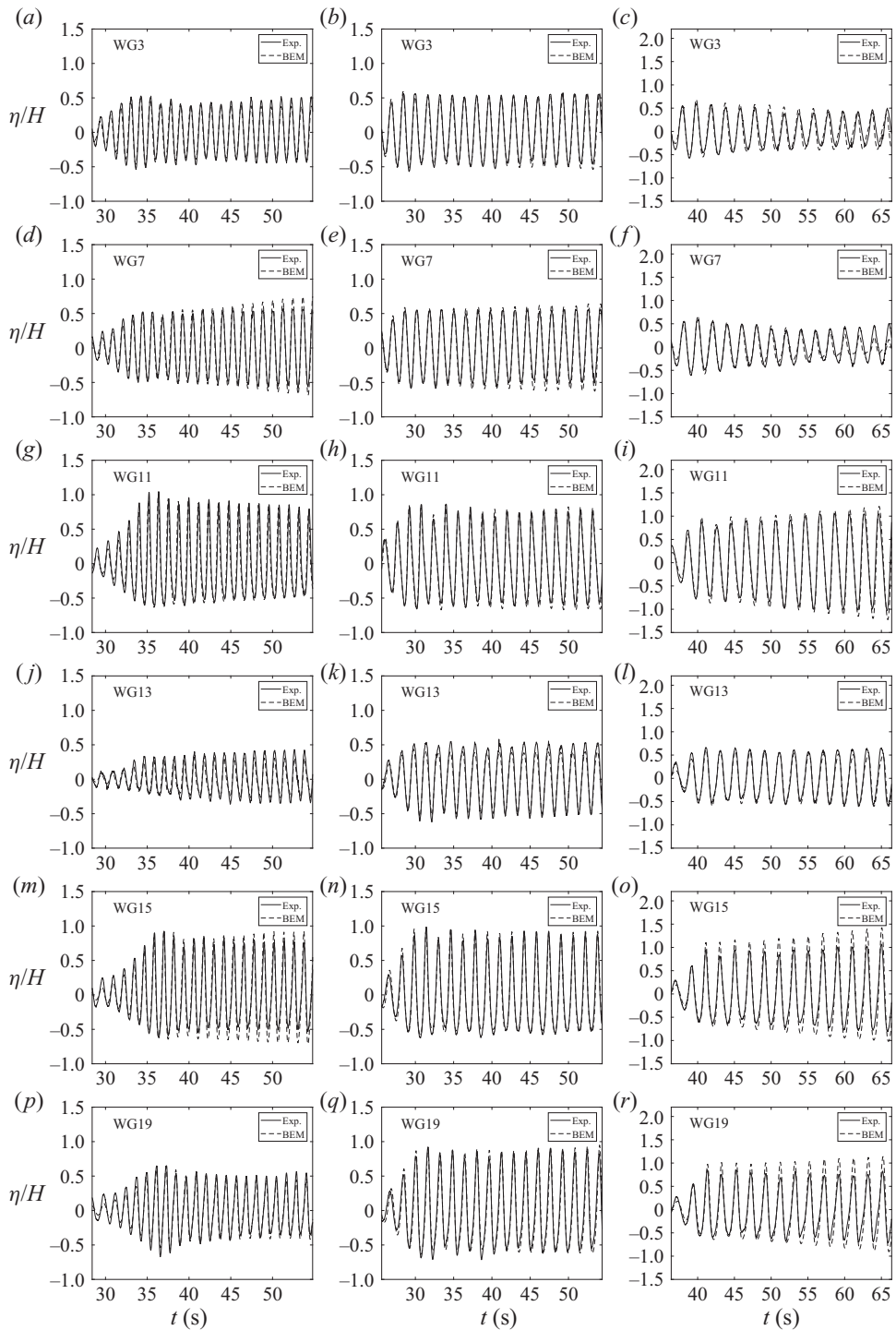
Figure 5. Comparison of the free-surface elevation at six selected WGs (WG3, 7, 11, 13, 15, 19) when $B =$ 20 cm, $h = 50$ cm, $H/h = 0.1$: $T = 1.2$ s (*a,d,g,j,m,p*); $T = 1.6$ s (*b,e,h,k,n,q*); $T = 2$ s (*c,f,i,l,o,r*). The solid and dashed lines represent the experimental and numerical results, respectively.
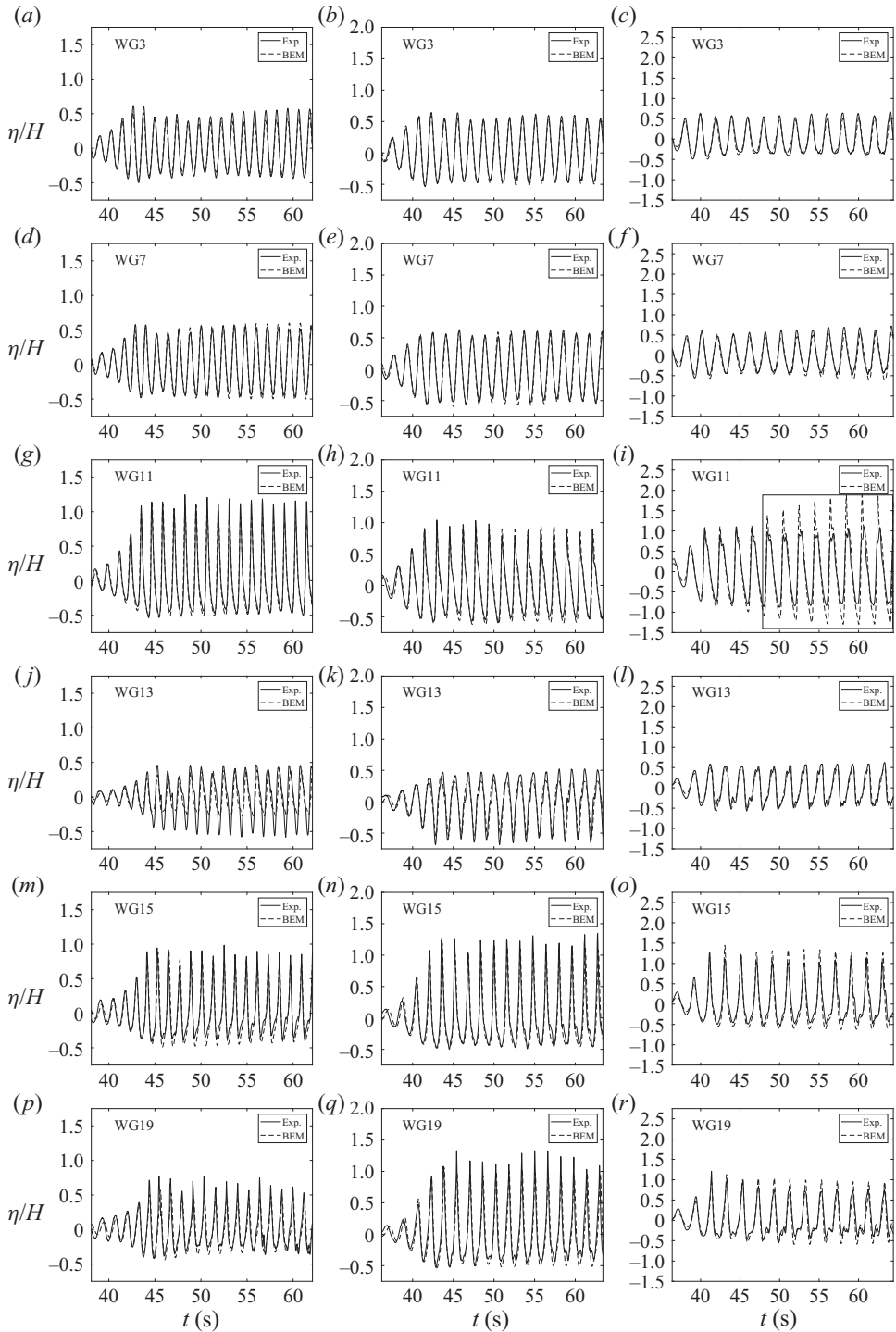
Figure 6. Same as figure 5 when $B = 30$ cm, $h = 60$ cm, $H/h = 0.2$. The box on the third line and third column indicates the largest discrepancy between experiments and simulations.

of figure 6 that corresponds to $T = 1.6$ s, the wave amplitudes at WGs 15 and 19 are even larger than that at WG11. This phenomenon depends on the ratio of the wave length to the length of the plate.

In figure 6, at WG19 for $T = 2$ s, one observes nonlinearities that are typical of reflected waves interacting with the incoming wave. There is a strong crest/trough asymmetry at WG11 for $T = 1.2$ s. The largest discrepancy between experiments and simulations occurs at WG11 when $T = 2$ s (see the box in the plot on the third line and third column of figure 6). The experimental values plateau while the numerical values keep increasing. The numerical values are the largest of all our simulations. The large amplitudes are due to 3-D effects leading to waves developing into jets that often characterize wave breaking in crossing seas. The topic of 3-D wave breaking has been recently revisited by McAllister *et al.* (2019), who showed experimentally the formation of upward projected jets that do not limit wave crest height under crossing-sea conditions. Longuet-Higgins & Dommermuth (2001*a,b*) also studied numerically the breaking of standing waves and the consequent formation of jets.

4.2. *Horizontal force, vertical force and moment*

The nonlinear hydrodynamic loads are calculated by integrating the pressure distribution along the structure's surface,

$$\boldsymbol{F} = \int p\boldsymbol{n}\,\mathrm{d}S, \tag{4.1}$$

$$\boldsymbol{M} = \int p\boldsymbol{x} \times \boldsymbol{n}\,\mathrm{d}S, \tag{4.2}$$

where $\boldsymbol{F}$ and $\boldsymbol{M}$ are the hydrodynamic force and moment, respectively, $\boldsymbol{x}$ is the vector of coordinates from the centre of the plate.

To obtain the pressure distribution on the structure, Bernoulli's equation is used:

$$\frac{p}{\rho} = -gz - \frac{1}{2}\boldsymbol{\nabla}\phi \cdot \boldsymbol{\nabla}\phi - \frac{\partial\phi}{\partial t}. \tag{4.3}$$

As anticipated because of the symmetries involved in the experiments and reproduced in the numerical simulations, it was checked that the lateral force F_y, the yaw moment M_z and the roll moment M_x are negligible. Therefore, this section presents the comparisons of the horizontal force F_x, the vertical force F_z and the (pitching) moment M_y between the numerical and the experimental results. The overall agreement is satisfactory except for the horizontal force F_x in the case when the wave period is $T = 1.2$ s and for the vertical force F_z when $T = 2$ s. Examples for $B = 20$ cm, $h = 50$ cm, $H/h = 0.1$ and $B = 30$ cm, $h = 60$ cm, $H/h = 0.2$ are shown in the top row of figure 7 ($T = 1.2$ s). We also show results for $T = 1.6$ s and $T = 2$ s in figures 8 and 9. We selected some other cases where poor agreement was obtained. In figure 10, the horizontal force in the experiment is much larger than the numerical force at the beginning. The reason why this is happening eludes us. A typical WG measurement is shown as well. It can been seen that the free-surface elevation at this particular WG (and in fact at all WGs – not shown in the figure) is small at the beginning.

The vertical force shows several different patterns, for example increasing in figure 11(*a,c*), and fluctuating like a wave group in figure 11(*b,d*). Since the pattern is not periodic, the maxima of the vertical forces cannot be defined, as opposed to the case of solitary waves, as shown in Geng *et al.* (2021).
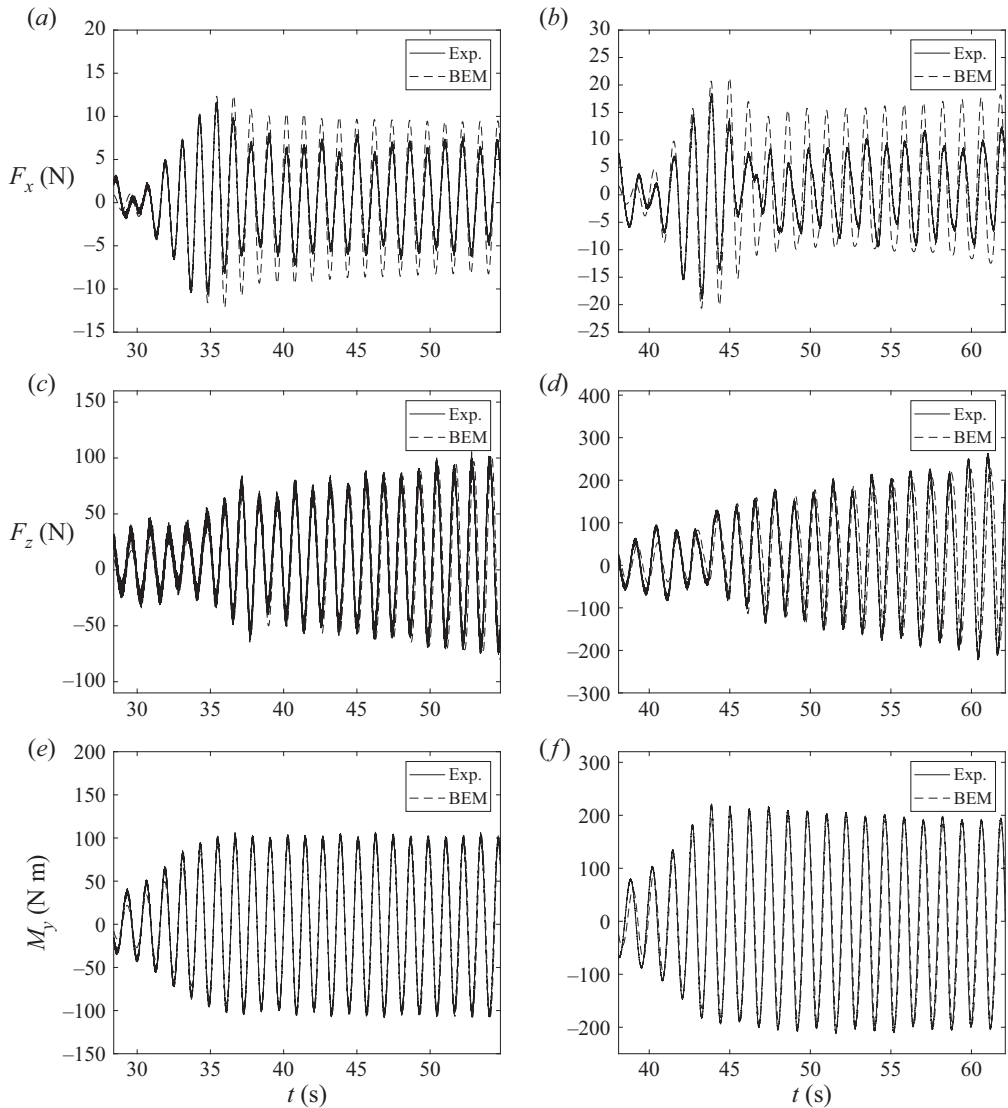
Figure 7. Horizontal force F_x (*a,b*), vertical force F_z (*c,d*) and moment M_y (*e,f*) when $B = 20$ cm, $h = 50$ cm, $H/h = 0.1$ (*a,c,e*) and $B = 30$ cm, $h = 60$ cm, $H/h = 0.2$ (*b,d,f*). Here $T = 1.2$ s (solid line, experimental; dashed line, numerical).

Unlike the vertical force, the time history of the pitching moment shows a consistent periodicity. Since the plate is relatively thin, the pressure distributions on the upper and lower faces are the key contributors to the moment. Compared with the variable behaviours that we highlighted for the vertical force, we can conjecture that the pressures also fluctuate along both sides of the plate but that the way they are distributed somehow maintains unchanged the magnitude of the moment.

4.3. *Description of the hydrodynamic loading process*

We choose the case $B = 30$ cm, $h = 60$ cm, $H/h = 0.1$, $T = 1.8$ s (see figure 12) to analyse the basic hydrodynamic loading process and how the reflected scattered waves

935 A23-12
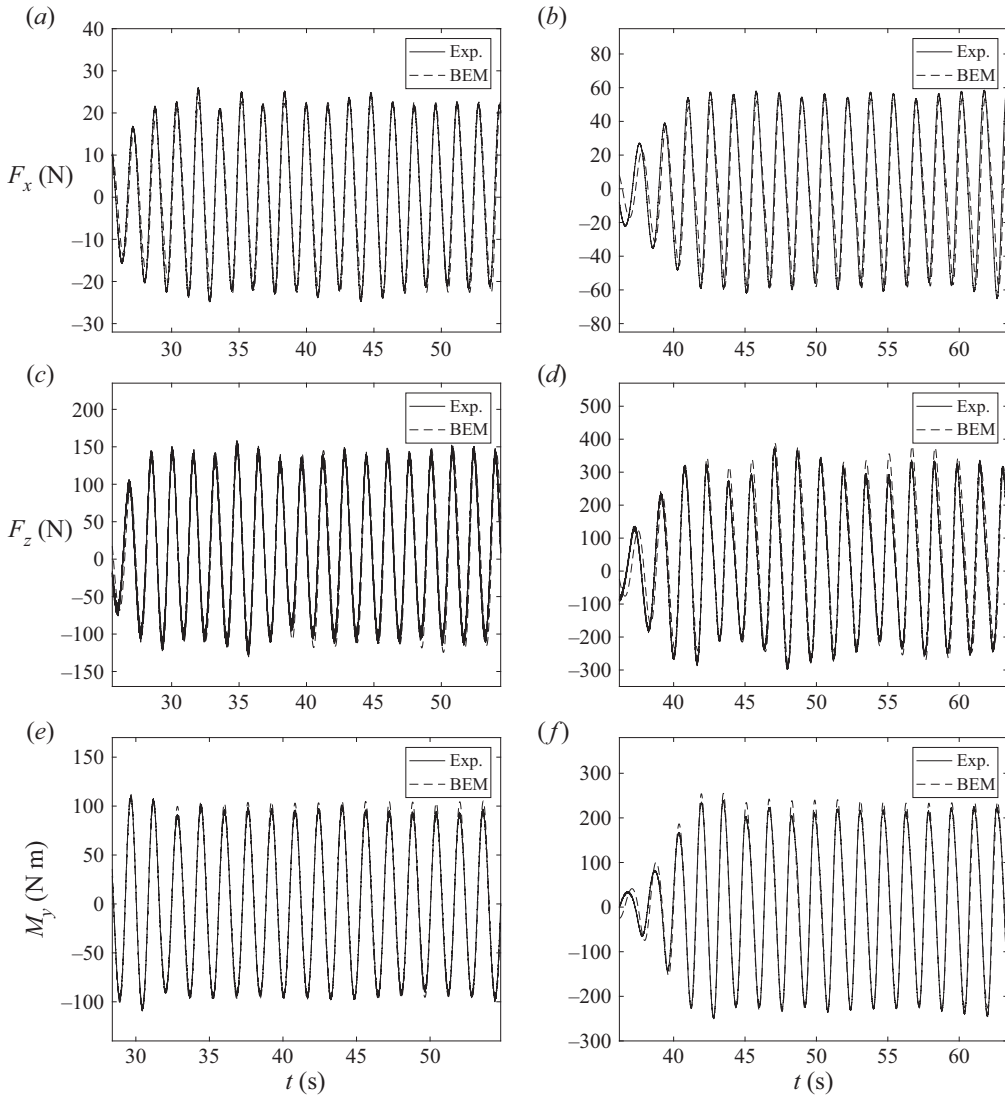
Figure 8. Same as figure 7 for $T = 1.6$ s.

alter the wave field. Selected time points are marked A, B, C, D, E and F. Figure 13 shows a sequence of numerical results at these key times of the loading process within one wave period.

The first column in figure 13 shows the pressure distribution in the middle line of the plate's upper and lower faces. If we define the upper surface pressure as P_{upper} and the lower surface pressure as P_{lower}, their difference is defined as $P_{lower} - P_{upper}$. The vertical force and pitching moment can be calculated from the following expressions:

$$F_z = \int_S (P_{lower} - P_{upper}) \, \mathrm{d}S, \quad M_y = \int_S (P_{lower} - P_{upper}) x \, \mathrm{d}S, \qquad (4.4a,b)$$

where S denotes the surface area of the plate.
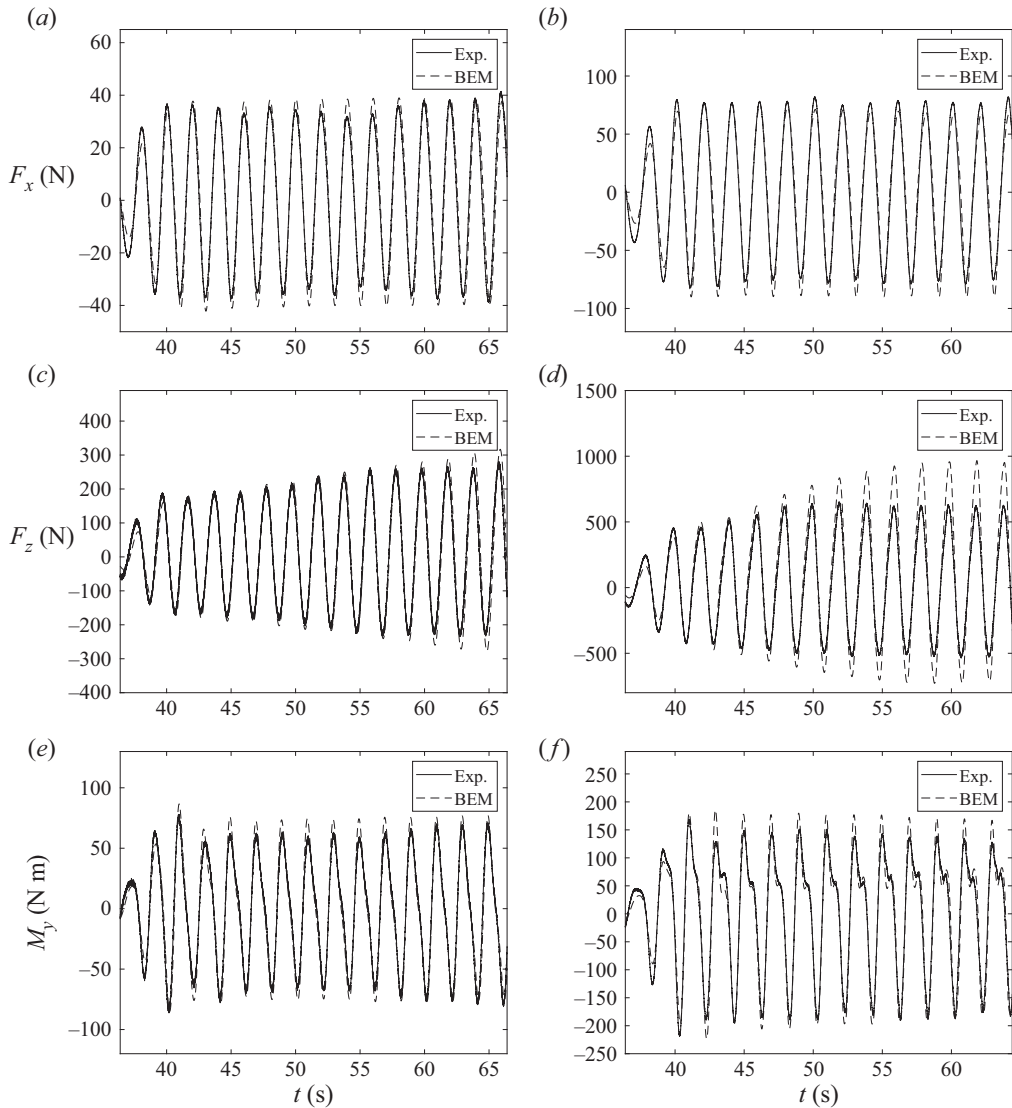
Figure 9. Same as figure 7 for $T = 2$ s.

The loading process starts with the wave crest reaching the leading edge of the plate. The previous wave cycle leaves a hollow on the free surface and a low pressure area covering almost half of the trailing edge side of the plate, which leads to the maximum vertical force. As the wave propagates, it focuses above the plate and alters the upper surface pressure distribution, leading to the minimum moment and the zero-crossing point for the vertical force subsequently. When the centre of the focused wave is moving close to the centre of the plate, the pressure distribution is balanced on both sides, which yields the zero-crossing point for the moment. Wave focusing continues and leads to an increase of the upper surface pressure even further, giving the minimum vertical force. In the end, the focused wave reaches its peak near the trailing edge and is ready to decrease and leave the plate.

935 A23-14
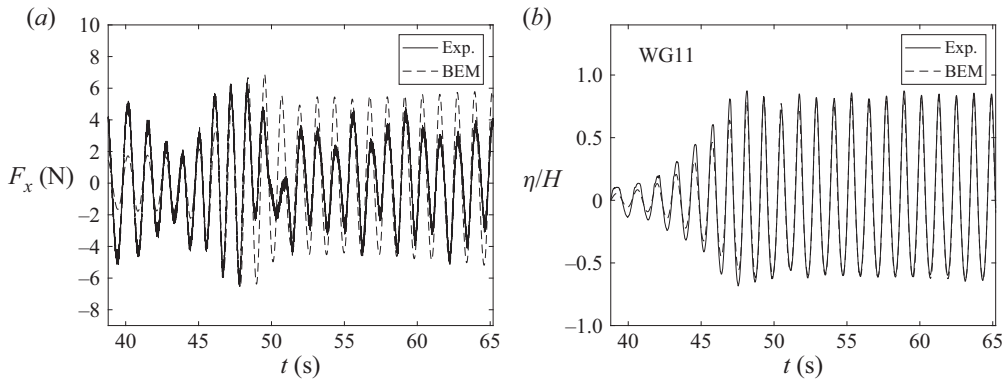
Figure 10. Horizontal force F_x and free-surface elevation at WG11 when $B = 20$ cm, $h = 60$ cm, $H/h = 0.1$, $T = 1.2$ s (solid line, experimental; dashed line, numerical).
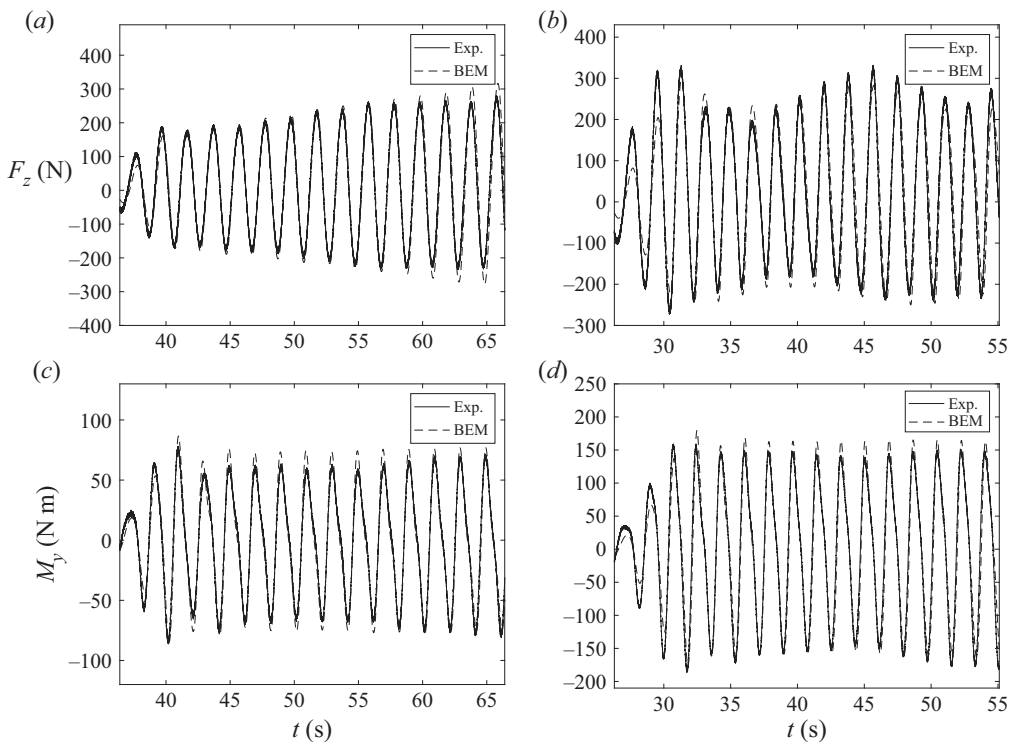
Figure 11. Vertical force F_z and moment M_y when $B = 20$ cm, $h = 50$ cm, $H/h = 0.1$, $T = 2$ s (a,c) and $B = 20$ cm, $h = 50$ cm, $H/h = 0.2$, $T = 1.8$ s (b,d) (solid line, experimental; dashed line, numerical).

By analysing the basic loading process, it can be seen that the ratio of the wavelength to the plate length is a key parameter. Different ratios mean different relative positions of the focused wave above the plate, which has a great impact on the moment exerted on the plate.

To analyse how the lateral walls change the hydrodynamic load on the plate, we mark with letters I to VI several times of interest in figure 14. The pressure distribution along the plate at times corresponding to points I and VI is presented in figure 15. It can be
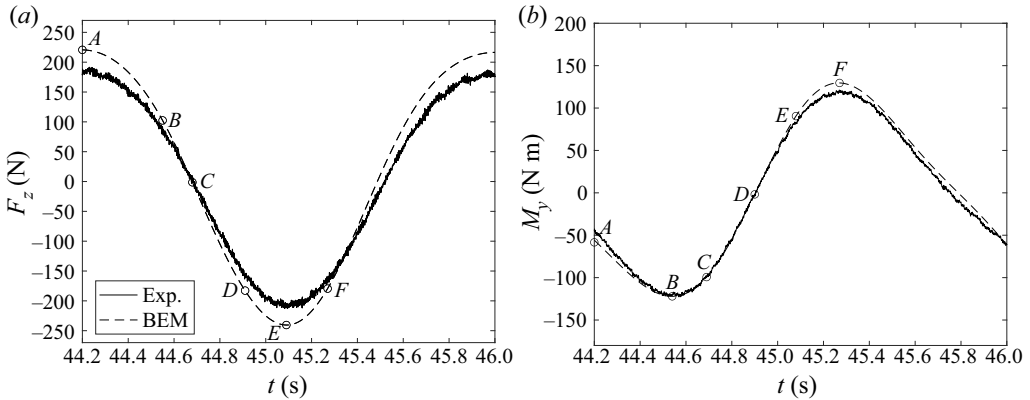
Figure 12. Selected times over one wave period for the vertical force (*a*) and the moment (*b*): A, maximum of F_z; B, minimum of M_y; C, zero-crossing of F_z; D, zero-crossing of M_y; E, minimum of F_z; F, maximum of F_y (solid line, experimental; dashed line, numerical). The parameters are $B = 30$ cm, $h = 60$ cm, $H/h = 0.1$, $T = 1.8$ s.

seen that from the time corresponding to point I to the time corresponding to point VI the pressures on both surfaces increase together but their differences decrease. However, the change of the pressure difference is almost symmetrically distributed along the plate. Combining these two effects explains why the amplitude of the vertical force decreases while the magnitude of the moment remains unchanged.

4.4. *Parametric study*

Since the results in the previous sections showed an overall good agreement between experimental and numerical results, we now investigate the effects of different parameters on the hydrodynamic loading process. One of the key parameters is the ratio between the wavelength and the width of the channel defined by

$$\lambda = \frac{\lambda'}{b'}, \tag{4.5}$$

where λ' is the wavelength, b' is the width of the channel and λ is the non-dimensional wavelength. As shown by Renzi & Dias (2012), the hydrodynamic behaviour varies at special values of λ, i.e. $\lambda = 1, 1/2, 1/3, \ldots$, which are known as the cutoff wavelengths of the transverse sloshing modes in a channel (see, for example, Shemer, Kit & Miloh 1986). The sloshing modes are transverse standing waves bouncing back and forth between the lateral walls. They have a wave length λ'_m related to the channel width b', satisfying $m\lambda'_m/2 = b'$. Due to the symmetry of our problem, we only have the even sloshing modes. The first two even modes are plotted in figure 16. In the following discussion, the width of the channel b' is fixed as 4 m and the water depth is set to be 60 cm. The wavelengths of the first two sloshing modes are $\lambda'_2 = 4$ and $\lambda'_4 = 2$ m. Their corresponding wave periods are 1.8653 and 1.1582 s. To demonstrate that the frequency of the first sloshing mode is not related to the incoming wave, we show in figure 17 the spectrum of the wave elevation at WG11 when the wave period is 1.4 s. As can be seen, the frequency of the first sloshing mode, around 0.536 Hz ($T = 1.8653$ s), is captured apart from the main frequency of the incoming wave.

935 A23-16
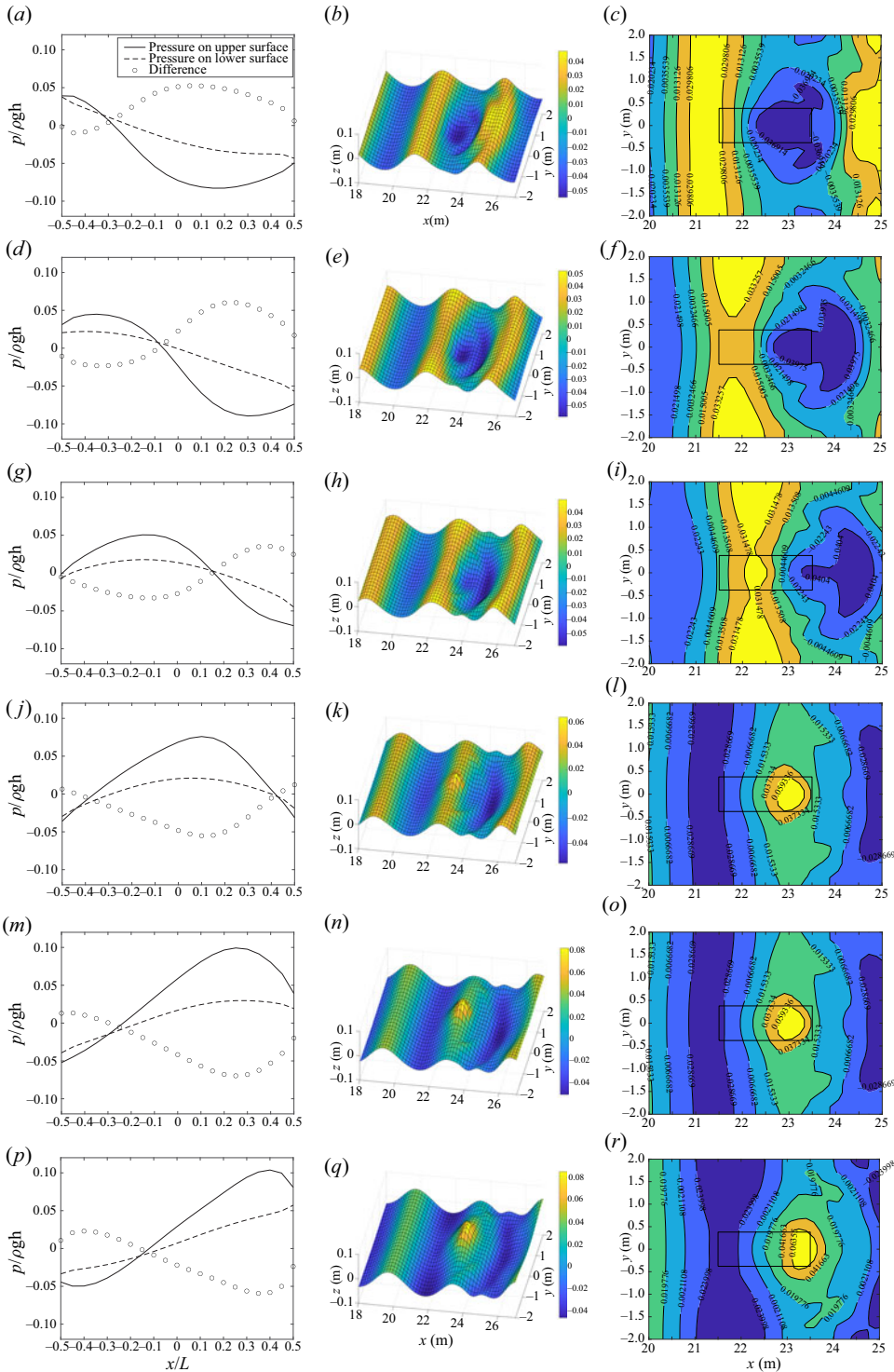
Figure 13. Sequence of numerical results illustrating the loading process. The parameters are $B = 30$ cm, $h = 60$ cm, $H/h = 0.1$, $T = 1.8$ s. (*a,d,g,j,m,p*) Pressure distribution on the upper and lower faces of the plate and their difference; (*b,e,h,k,n,q*) snapshot of the free surface; (*c,f,i,l,o,r*) top view of the free surface. See figure 12 for the significance of the times A–F.
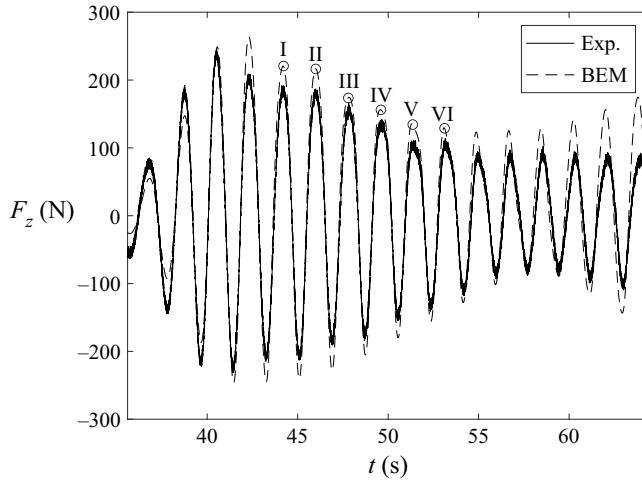
Figure 14. Vertical force F_z showing a decreasing trend when $B = 30$ cm, $h = 60$ cm, $H/h = 0.1$, $T = 1.8$ s (solid line, experimental; dashed line, numerical).
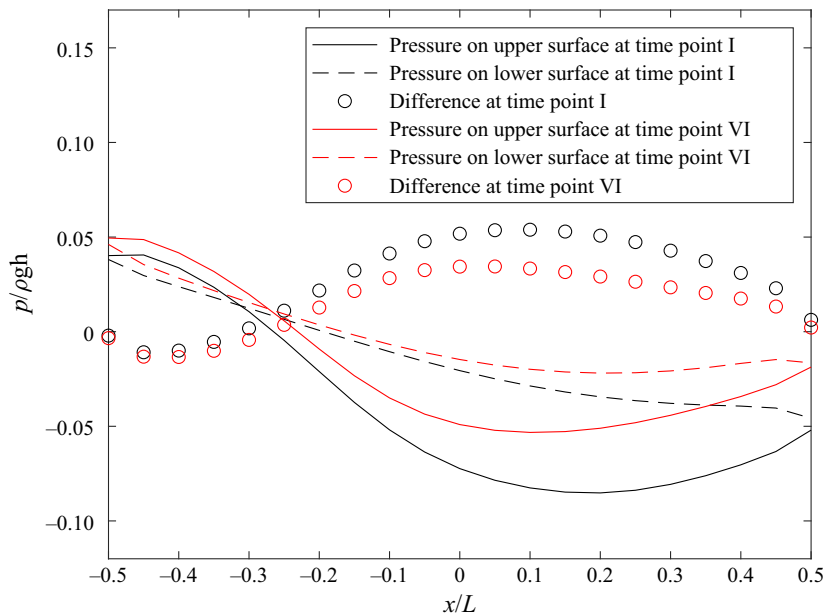
Figure 15. Numerically calculated pressure distribution at times corresponding to points I and VI (solid line, pressure distribution on the upper face of the plate; dashed line, pressure distribution on the lower face of the plate).

To understand how the sloshing modes affect the hydrodynamic behaviour at these cutoff wavelengths, two representative cases are investigated: $\lambda = 1$ and $\lambda = 1/2$ when $B = 30$ cm, $h = 60$ cm and $H/h = 0.1$.

Figure 18 shows the free-surface elevations around the plate when $\lambda = 1/2$. It can be seen that wave focusing above the plate is intensified and the wave amplitude at WG13 is compressed. A physical interpretation is that the transverse sloshing mode when $m = 4$ shares the same frequency as that of the propagating wave while its phase coincides, so

935 A23-18
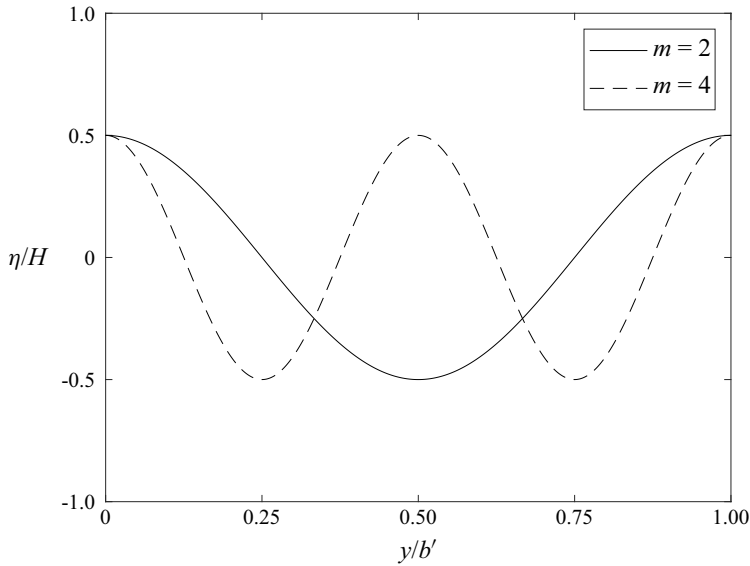
Figure 16. The first two even sloshing modes (solid line, $m = 2$; dashed line, $m = 4$).
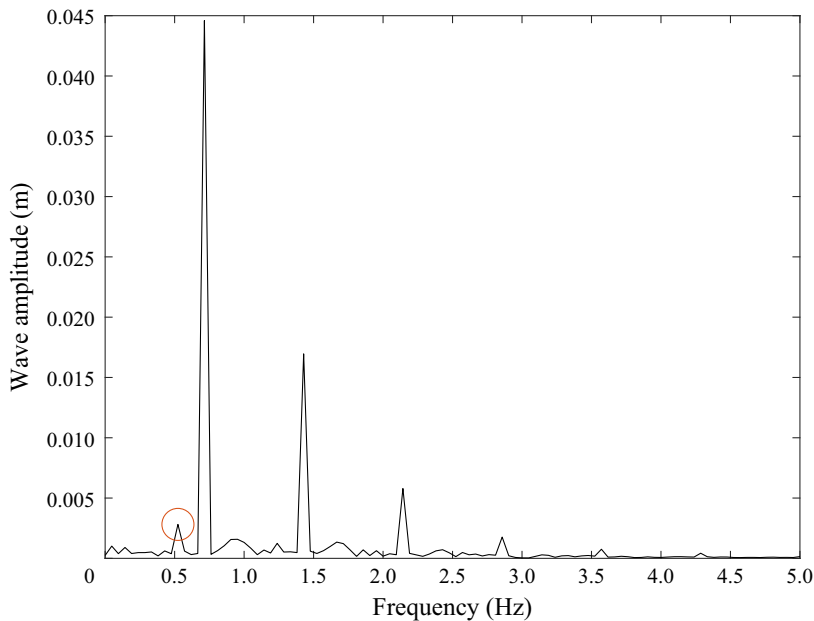
Figure 17. Fourier analysis of the wave elevation at WG11 when $B = 30$ cm, $h = 60$ cm, $H/h = 0.1$ and $T = 1.6$ s. The red circle indicates the frequency of the first sloshing mode.

that when the standing wave reaches its peak in the middle line, the propagating wave also reaches its crest. When this sloshing mode reaches its crest in the centre, it has a trough at one quarter of the channel and cancels the crest of the incoming wave. Because WG13 is located close to that point, it explains why the free-surface elevation at WG13 is compressed. To illustrate the effects of this transverse sloshing mode more clearly, we plot
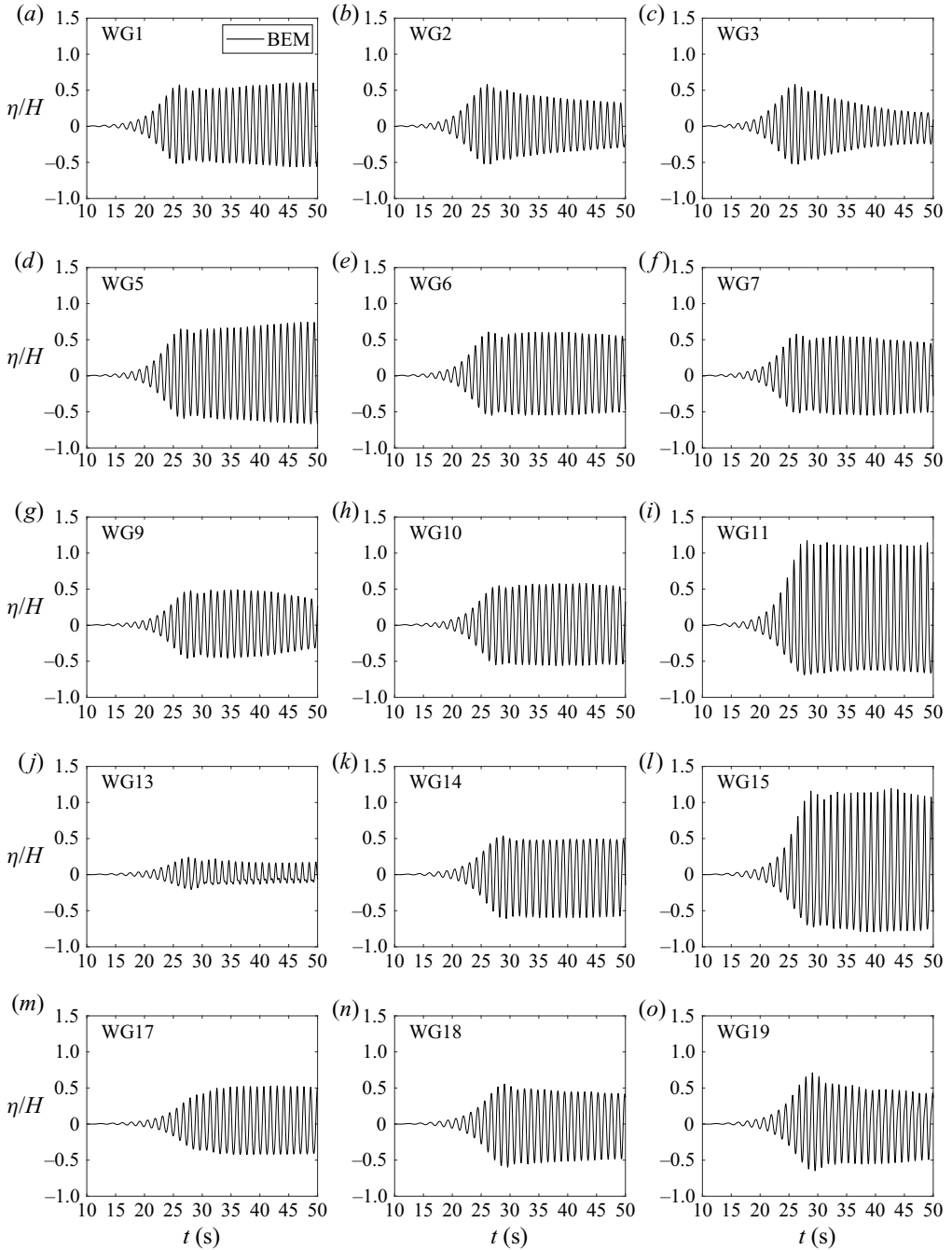
Figure 18. Free-surface elevation at 15 selected WGs when $B = 30$ cm, $h = 60$ cm, $H/h = 0.1$, $\lambda = 1/2$, $T = 1.1582$ s.
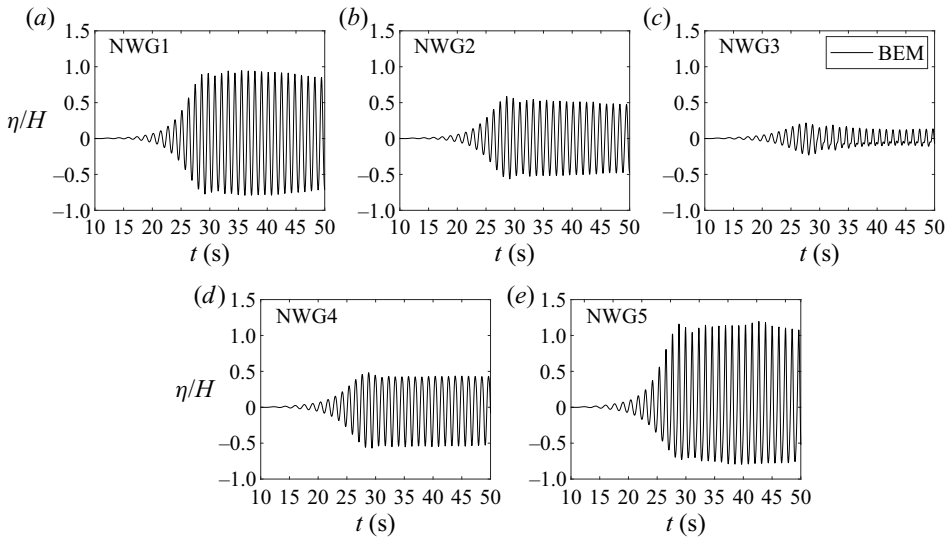
Figure 19. Free-surface elevation at five additional numerical WGs given in table 5 when $B = 30$ cm, $h = 60$ cm, $H/h = 0.1$, $\lambda = 1/2$, $T = 1.1582$ s.

NWG1 $(105, -195)$ NWG2 $(105, -150)$ NWG3 $(105, -100)$ NWG4 $(105, -50)$ NWG5 $(105, 0)$

Table 5. Additional numerical WG coordinates.

the elevations at additional numerical WGs that correspond to the nodes and antinodes of the standing wave (see figure 19 and table 5). It can be seen that the wave amplitude of these five numerical WGs follows the standing wave pattern, which also demonstrates the resonance between the incoming wave and the transverse sloshing mode.

Figures 20 and 21 show the free-surface elevations around the plate when $\lambda = 1$. The resonant behaviour present in the case $\lambda = 1/2$ is no longer present. This is due to the phase difference between the sloshing mode when $m = 2$ and the incoming wave, even though these two components have the same frequency. The phase difference between the sloshing mode and the incoming wave is determined by the speed of the scattered wave travelling to the lateral walls and the distance between the plate and lateral walls. The hydrodynamic loads when $\lambda = 1/2$ and $\lambda = 1$ are plotted in figure 22. Due to the resonance, the vertical force increases abruptly at some point when $\lambda = 1/2$.

As shown in figure 23, the interaction between the sloshing modes and the incoming wave always occurs on the downstream side of the plate. Since in these two cases the length of the plate is fixed at 2 m, it is possible that this complex interaction will have little effect on the hydrodynamic loads in the case of a wavelength of 4 m ($\lambda = 1$). To illustrate this, two more numerical experiments are conducted. We fix both the length of the plate and the wavelength at 4 m. The other parameters remain unchanged except that the widths of the channel are set at 4 and 8 m. The vertical forces exerted on the plate are shown in figure 24. When the width of the channel is equal to 4 m, we see from the vertical force that at the beginning the sloshing mode is not established yet. Then it gradually develops and starts to change the hydrodynamic load completely. In this case $\lambda = 1$, the only parameter that changes is the length of the plate from 2–4 m. It is yet more evidence that the complex
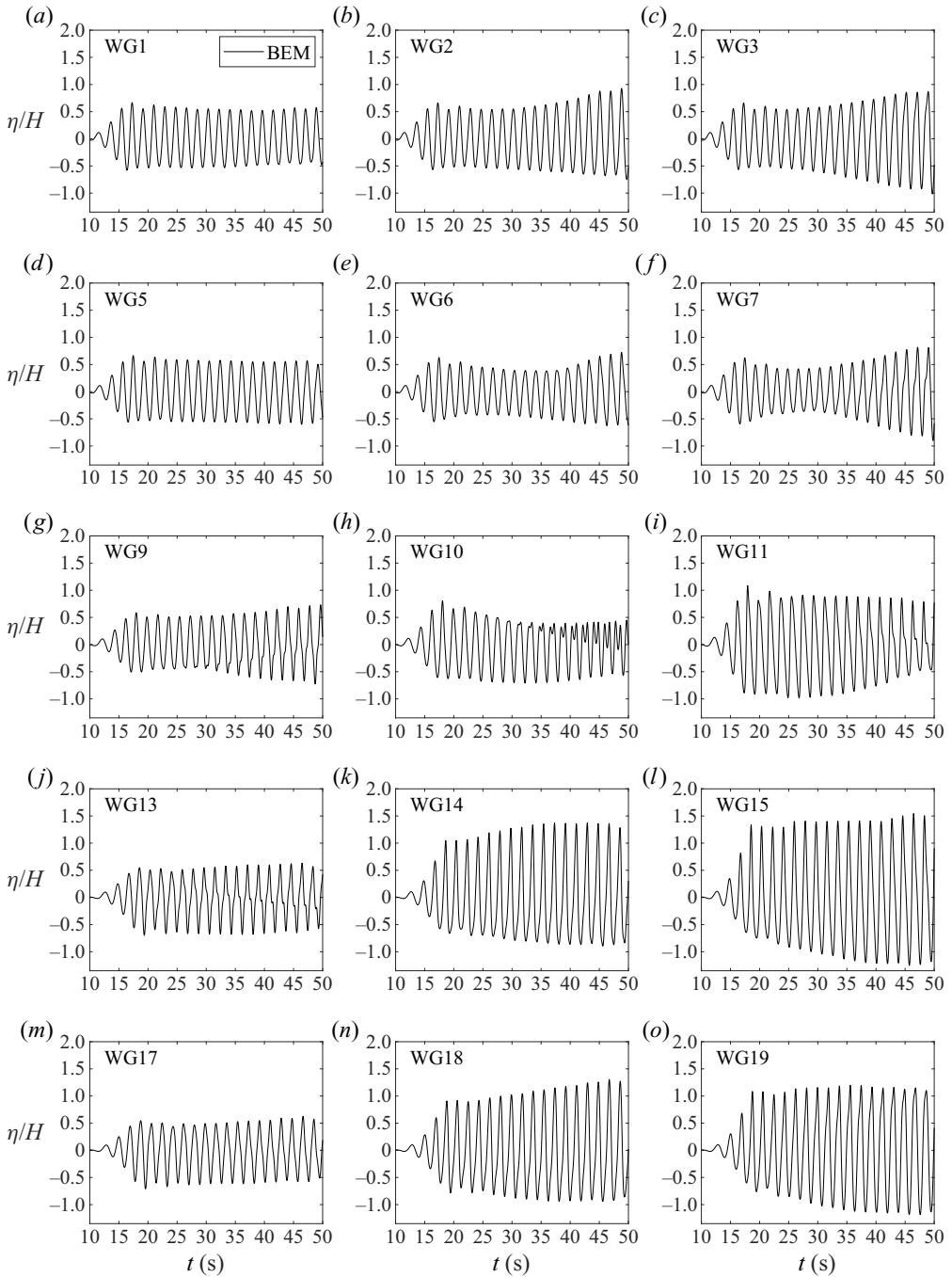
Figure 20. Free-surface elevation at 15 selected WGs when $B = 30$ cm, $h = 60$ cm, $H/h = 0.1$, $\lambda = 1$, $T = 1.8653$ s.
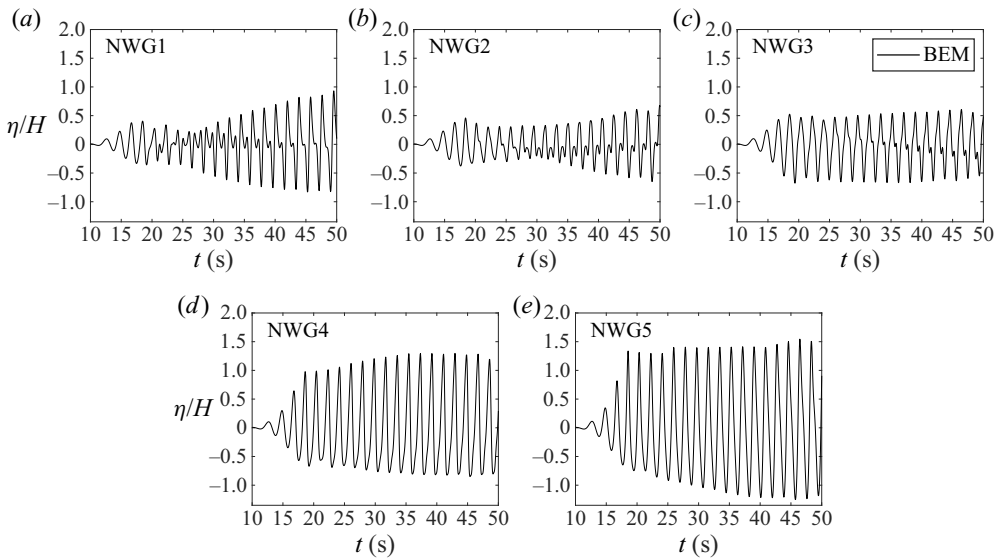
Figure 21. Free-surface elevation at five additional numerical WGs given in table 5 when $B = 30$ cm, $h = 60$ cm, $H/h = 0.1$, $\lambda = 1$, $T = 1.8653$ s.

interaction happens on the downstream side. By increasing the length of the plate, we enable the interaction to have a great impact on the hydrodynamic load on the plate.

Comparing the hydrodynamic loads in two different channel widths in figure 24, we find that the vertical force amplitude when the channel width is equal to 4 m is almost double the one when the width is equal to 8 m. One can imagine that when the width of the channel is equal to the width of the plate, the problem becomes purely 2-D. On the other hand, when the width of the channel goes to infinity, the problem tends to that of open-sea conditions.

5. Discussion and conclusion

Wave scattering by a 3-D submerged horizontal plate in a channel was investigated both experimentally and numerically. While several studies of the 2-D problem can be found in the literature, the 3-D problem has been essentially untouched. It is clear that the flow and the loads differ in the 3-D context. For the 3-D problem, the pressure distribution on the lower surface is very sensitive to the phase difference between the sloshing mode generated by the presence of the plate and the incoming wave. This phase difference is determined by the speed of the scattered wave travelling to the lateral walls and the distance between the plate and lateral walls. Numerical results show that the pressure distribution differs from the linear distribution from the leading edge to the trailing edge that can be revealed from the 2-D problem (Lo & Liu 2014). Additionally, a local hump and a pit appear near the crest and the trough of the waves, respectively, propagating over the submerged plate of finite span.

The agreement between experiments and simulations was found to be good overall, even if some discrepancies were observed. Because of that, we were also able to consider numerically more cases than were considered experimentally. In particular, we studied the effect of the channel width. It is important to understand this effect since submerged plates can be found either in the open ocean or inside harbours and naturally formed confined
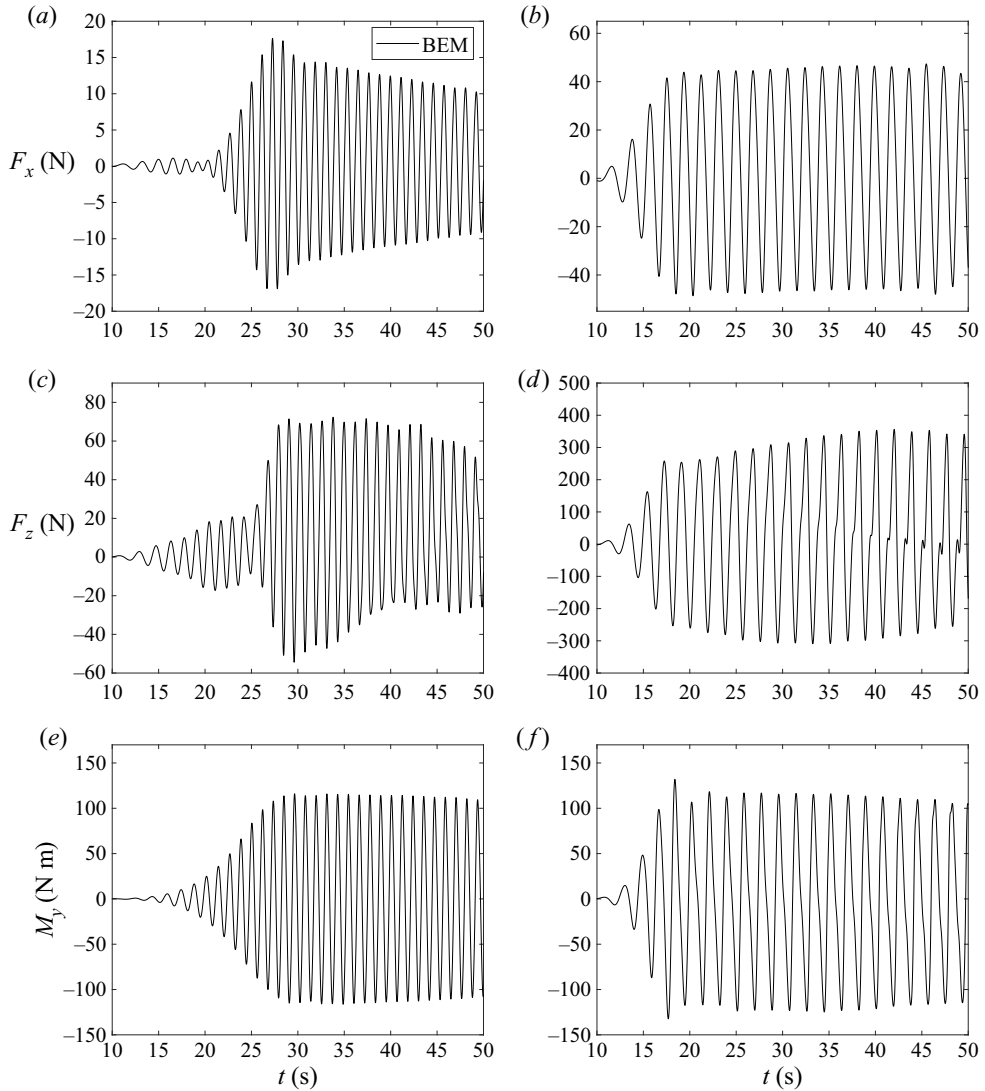
Figure 22. Horizontal force F_x, vertical force F_z and moment M_y when $B = 30$ cm, $h = 60$ cm, $H/h = 0.1$: $\lambda = 1/2$, $T = 1.1582$ s (a,c,e) and $\lambda = 1$, $T = 1.8653$ s (b,d,f).

offshore areas. Resonances can occur, leading to modified loads on the plate. It is clear that care should be taken when employing the results obtained in a wave tank to predict the loading of the plate in the open ocean. The same comment was made by Renzi & Dias (2013) in their study of wave energy converters, and in particular of oscillating wave surge converters having the shape of a plate. In ocean engineering, wave scattering by offshore structures under open-sea conditions is usually studied experimentally in a wide tank. The scattered wave field is absorbed by active absorption wavemakers at all boundaries. The wave generation process continues until a steady state is reached. However, in the experiments presented here, the scattered wave field is reflected by the lateral walls to investigate channel effects rather than being absorbed. The reflected wave field keeps propagating both upstream and downstream and eventually changes the characteristics
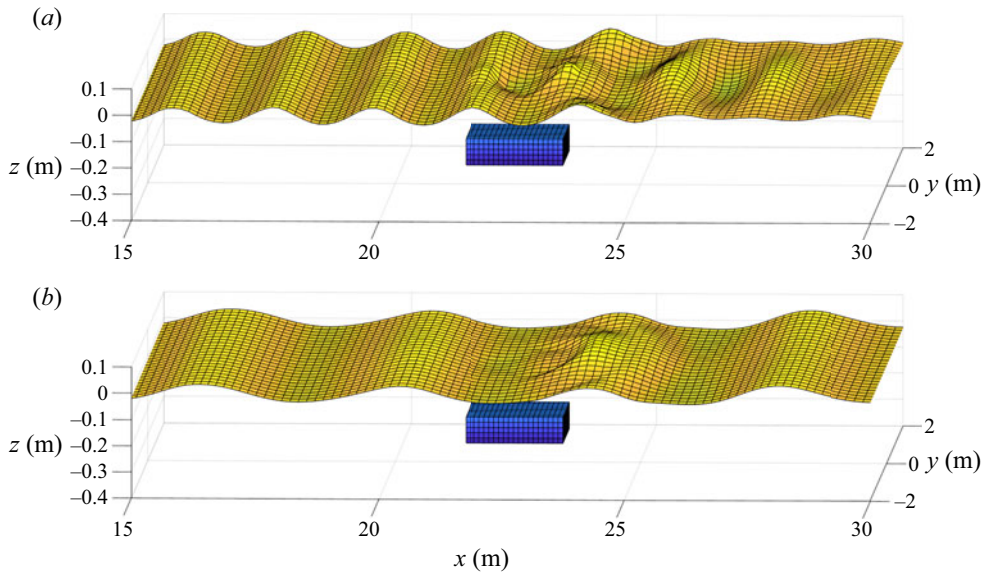
Figure 23. Snapshots of free surface when $\lambda = 1/2$ and $\lambda = 1$.
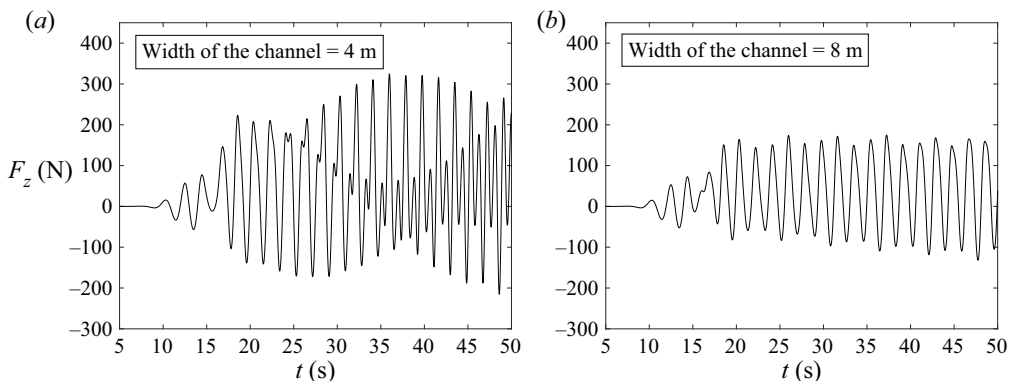
Figure 24. Vertical force exerted on the plate when the channel widths are equal to 4 m (*a*) and 8 m (*b*).

of the incoming regular waves. Therefore, the experimental method used in wide tanks cannot be applied in our case.

In the present framework of a submerged horizontal plate, we were also able to study the effect of the thickness of the plate in a companion paper by Geng *et al.* (2021) that was restricted to solitary waves. Since the effect was found to be weak, it was not considered in the present paper. The other effect that was not considered in the present paper is the effect of wave breaking. Indeed, the potential flow solver that we used does not allow us to simulate cases where the incoming wave breaks when it hits the plate. A CFD solver should then be used. This is left for future work.

Author ORCIDs.

H. Liu https://orcid.org/0000-0003-2060-5819;

F. Dias https://orcid.org/0000-0002-5123-4929.

REFERENCES

BROSSARD, J. & CHAGDALI, M. 2001 Experimental investigation of the harmonic generation by waves over a submerged plate. *Coast. Engng* **42** (4), 277–290.

CHEONG, H.F., SHANKAR, N.J. & NALLAYARASU, S. 1996 Analysis of submerged platform breakwater by eigenfunction expansion method. *Ocean Engng* **23** (8), 649–666.

DEAN, R.G. & DALRYMPLE, R.A. 1991 *Water Wave Mechanics for Engineers and Scientists*, vol. 2. World Scientific Publishing Company.

DONG, J., WANG, B., ZHAO, X. & LIU, H 2018 Wave forces exerted on a submerged horizontal plate over an uneven bottom. *J. Engng Mech. ASCE* **144** (6), 04018030.

FARINA, L. & MARTIN, P.A. 1998 Scattering of water waves by a submerged disc using a hypersingular integral equation. *Appl. Ocean Res.* **20** (3), 121–134.

GENG, T., LIU, H. & DIAS, F. 2021 Solitary-wave loads on a three-dimensional submerged horizontal plate: numerical computations and comparison with experiments. *Phys. Fluids* **33**, 037129.

GRILLI, S.T., GUYENNE, P. & DIAS, F. 2001 A fully non linear model for three dimensional overturning waves over an arbitrary bottom. *Intl J. Numer. Meth. Fluids* **35** (7), 829–867.

GRILLI, S.T., DIAS, F., GUYENNE, P., FOCHESATO, C. & ENET, F. 2010 Progress in fully nonlinear potential flow modeling of 3D extreme ocean waves. In *Advances in Numerical Simulation of Nonlinear Water Waves (Q. Ma)*, pp. 75–28. World Sci.

KOJIMA, H., YOSHIDA, A. & NAKAMURA, T. 1994 Linear and nonlinear wave forces exerted on a submerged horizontal plate. In *Proceedings of 24th Conference on Coastal Engineering, Kobe, Japan*, pp. 1312–1326.

LIAM, L.S, ADYTIA, D. & VAN GROESEN, E. 2014 Embedded wave generation for dispersive surface wave models. *Ocean Engng* **80**, 73–83.

LIU, P.L.F. & ISKANDARANI, M. 1991 Scattering of short-wave groups by submerged horizontal plate. *ASCE J. Waterway Port Coastal Ocean Engng* **117** (3), 235–246.

LIU, C., HUANG, Z. & TAN, S.K. 2009 Nonlinear scattering of non-breaking waves by a submerged horizontal plate: experiments and simulations. *Ocean Engng* **36** (17–18), 1332–1345.

LO, H.Y. & LIU, P.L.F. 2014 Solitary waves incident on a submerged horizontal plate. *ASCE J. Waterway Port Coastal Ocean Engng* **140** (3), 04014009.

LONGUET-HIGGINS, M.S. & DOMMERMUTH, D.G. 2001a On the breaking of standing waves by falling jets. *Phys. Fluids* **13**, 1652–1659.

LONGUET-HIGGINS, M.S. & DOMMERMUTH, D.G. 2001b Vertical jets from standing waves II. *Proc. R. Soc. Lond.* A **457**, 2137–2149.

MCALLISTER, M.L., DRAYCOTT, S., ADCOCK, T.A.A., TAYLOR, P.H. & VAN DEN BREMER, T.S. 2019 Laboratory recreation of the Draupner wave and the role of breaking in crossing seas. *J. Fluid Mech.* **860**, 767–786.

PARSONS, N.F. & MARTIN, P.A. 1992 Scattering of water waves by submerged plates using hypersingular integral equations. *Appl. Ocean Res.* **14** (5), 313–321.

PATARAPANICH, M. 1984 Forces and moment on a horizontal plate due to wave scattering. *Coast. Engng* **8** (3), 279–301.

PATARAPANICH, M. & CHEONG, H.F. 1989 Reflection and transmission characteristics of regular and random waves from a submerged horizontal plate. *Coast. Engng* **13** (2), 161–182.

PINON, G., PERRET, G., CAO, L., POUPARDIN, A., BROSSARD, J. & RIVOALEN, E. 2017 Vortex kinematics around a submerged plate under water waves. Part II: numerical computations. *Eur. J. Mech. (B/Fluids)* **65**, 368–383.

POUPARDIN, A., PERRET, G.G.N.E., PINON, G., BOURNETON, N., RIVOALEN, E. & BROSSARD, J. 2017 Vortex kinematic around a submerged plate under water waves. Part I: experimental analysis. *Eur. J. Mech. (B/Fluids)* **34**, 47–55.

RENZI, E. & DIAS, F. 2012 Resonant behaviour of an oscillating wave energy converter in a channel. *J. Fluid Mech.* **701**, 482–510.

RENZI, E. & DIAS, F. 2013 Hydrodynamics of the oscillating wave surge converter in the open ocean. *Eur. J. Mech. (B/Fluids)* **41**, 1–10.

SHEMER, L., KIT, E. & MILOH, T. 1986 Measurements of two-and three-dimensional waves in a channel, including the vicinity of cut-off frequencies. *Exp. Fluids* **5** (1), 66–72.

SIEW, P.F. & HURLEY, D.G 1977 Long surface waves incident on a submerged horizontal plate. *J. Fluid Mech.* **83** (1), 141–151.

WANG, Q., FANG, Y.L. & LIU, H. 2018 Physical generation of Tsunami waves in offshore region. *J. Earthq. Tsunami* **12** (02), 1840003.

WANG, Q., LIU, H., FANG, Y. & DIAS, F. 2020 Experimental study on free-surface deformation and forces on a finite submerged plate induced by a solitary wave. *Phys. Fluids* **32** (8), 086601.

YAN, S. & MA, Q.W. 2007 Numerical simulation of fully nonlinear interaction between steep waves and 2D floating bodies using the QALE-FEM method. *J. Comput. Phys.* **221** (2), 666–692.

YU, X. & CHWANG, A.T. 1993 Analysis of wave scattering by submerged circular disk. *J. Engng Mech. ASCE* **119** (9), 1804–1817.